ARTICLE OPEN

Check for updates

Phonon mixing in the charge density wave state of ScV_6Sn_6

Yanhong Gu[1], Ethan T. Ritz[2], William R. Meier[3], Avery Blockmon[1], Kevin Smith[1], Richa Pokharel Madhogaria[3], Shirin Mozaffari[3], David Mandrus[3,4,5], Turan Birol[2] and Janice L. Musfeldt[1,4]✉

Kagomé metals are widely recognized, versatile platforms for exploring topological properties, unconventional electronic correlations, magnetic frustration, and superconductivity. In the RV_6Sn_6 family of materials (R = Sc, Y, Lu), ScV_6Sn_6 hosts an unusual charge density wave ground state as well as structural similarities with the AV_3Sb_5 system (A = K, Cs, Rb). In this work, we combine Raman scattering spectroscopy with first-principles lattice dynamics calculations to reveal phonon mixing processes in the charge density wave state of ScV_6Sn_6. In the low temperature phase, we find at least four new peaks in the vicinity of the V-containing totally symmetric mode near 240 cm^{-1} suggesting that the density wave acts to mix modes of $P6/mmm$ and $R\bar{3}m$ symmetry - a result that we quantify by projecting phonons of the high symmetry state onto those of the lower symmetry structure. We also test the stability of the short-range ordered density wave state under compression and propose that both physical and chemical pressure quench the effect. We discuss these findings in terms of symmetry and the structure-property trends that can be unraveled in this system.

npj Quantum Materials (2023)8:58 ; https://doi.org/10.1038/s41535-023-00590-7

INTRODUCTION

Kagomé materials possess two-dimensional periodic networks of corner-sharing triangles and, as a result, exhibit a high degree of geometrical frustration. This structural frustration can create Dirac cones and flat bands in the electronic structure[1–5] as well as exotic magnetic ground states[6–8] accompanied by the anomalous Hall effect[9–12], charge fractionalization[13,14], chiral magnetism[15,16], and strong electron correlations[17]. The discovery of charge density waves (CDWs) in superconducting AV_3Sb_5 (A = K, Rb, Cs) and magnetic FeGe demonstrates that CDWs can exist in both magnetic and nonmagnetic kagomé lattices across a range of electron correlations[18–20]. At the same time, rich phase diagrams can be obtained by tuning the frustration and electron filling in the kagomé lattice. Strong entanglements make this platform well-suited to revealing intertwined and competing states.

Recently, a family of bi-layer analogs with chemical formula RV_6Sn_6 (R = Sc, Y, Lu, Tb, Ho, Gd...) has attracted attention [Fig. 1a][21]. These kagomé metals also host topological Dirac surface states, van Hove singularies, anisotropic magnetism, and other exciting properties[22,23]. Unlike all three AV_3Sb_5 compounds, superconductivity has not been reported in ScV_6Sn_6 under any temperature or pressure conditions investigated thus far[24,25], possibly due to the lack of a Γ-centered Fermi pocket in this material[26–29]. Further, only ScV_6Sn_6 exhibits a three dimensional CDW, making it comparable - at least in some ways - to the AV_3Sb_5's. Despite recent activity in this highly contemporary research area, there is much more to learn about the CDW in ScV_6Sn_6 and related materials. The combination of two kagomé layers per unit cell along with the lower symmetry CDW wavevector makes resolving structural details and the phase transition mechanism of ScV_6Sn_6 a particularly daunting task.

ScV_6Sn_6 is a paramagnetic metal with a first-order CDW transition at 92 K[25,30–32]. The long-range ordered CDW involves primarily out-of-plane Sc and Sn displacements; thus far, the contribution of the V centers has been considered to be small[25,33]. First-principles calculations point to lattice instabilities (soft modes) in ScV_6Sn_6[33] - possibly due to the small size of the Sc^{3+} radius. Experimentally, short-range order has been observed in the high temperature phase with wavevector (1/3, 1/3, 1/2)[31,32]. Stable long-range CDW order with wavevector (1/3, 1/3, 1/3) sets in below T_{CDW} = 92 K[25,31,32]. This type of lattice instability is not present in the Y and Lu analogs, and there are no CDWs in these materials[33].

Experimental confirmation of these findings by other probes is highly desirable. Traditionally, x-ray and vibrational spectroscopies have been used to unravel CDW mechanisms. Infrared and Raman scattering spectroscopies in particular are well-suited for exploring the microscopic aspects of local lattice distortions as well as phase and amplitude modes of a CDW. Of course, the metallic character of ScV_6Sn_6 challenges this approach because the odd-symmetry infrared-active phonons are screened by the Drude contribution[34]. Raman scattering provides a way forward[35], and it has been used to gain significant insight into CDWs in other kagomé systems[36,37] despite the fact that it accesses only even-symmetry excitations at the zone center. Naturally, ScV_6Sn_6 has more Raman-active modes than members of the AV_3Sb_5 family due to the larger unit cell.

An open question about ScV_6Sn_6 is why it has a different CDW wavevector than its better studied AV_3Sb_5 counterparts. Even if the driving force of the CDW instability were the same in these two families of vanadate kagomés, variations can arise from the electron count as well as the overall number of atoms in the unit cell thus producing distinct electronic structure near the Fermi level[38]. Furthermore, the apical Sb ions are important in determining the relative stability of CDW phases in CsV_3Sb_5[39]. This implies that the double-kagomé layer structure in ScV_6Sn_6 may impact the P vs. L point instabilities and, when they freeze in, their respective energy gains. Note that in this compound, instabilities both at the $P(\frac{1}{3}, \frac{1}{3}, \frac{1}{3})$ and $L(\frac{1}{2}, 0, \frac{1}{2})$ points are present.

[1]Department of Chemistry, University of Tennessee, Knoxville, TN 37996, USA. [2]Department of Chemical Engineering and Materials Science, University of Minnesota, Minneapolis, MN 55455, USA. [3]Materials Science and Engineering Department, University of Tennessee Knoxville, Knoxville, TN 37996, USA. [4]Department of Physics and Astronomy, University of Tennessee Knoxville, Knoxville, TN 37996, USA. [5]Materials Science and Technology Division, Oak Ridge National Laboratory, Oak Ridge, TN 37831, USA.
✉email: musfeldt@tennessee.edu

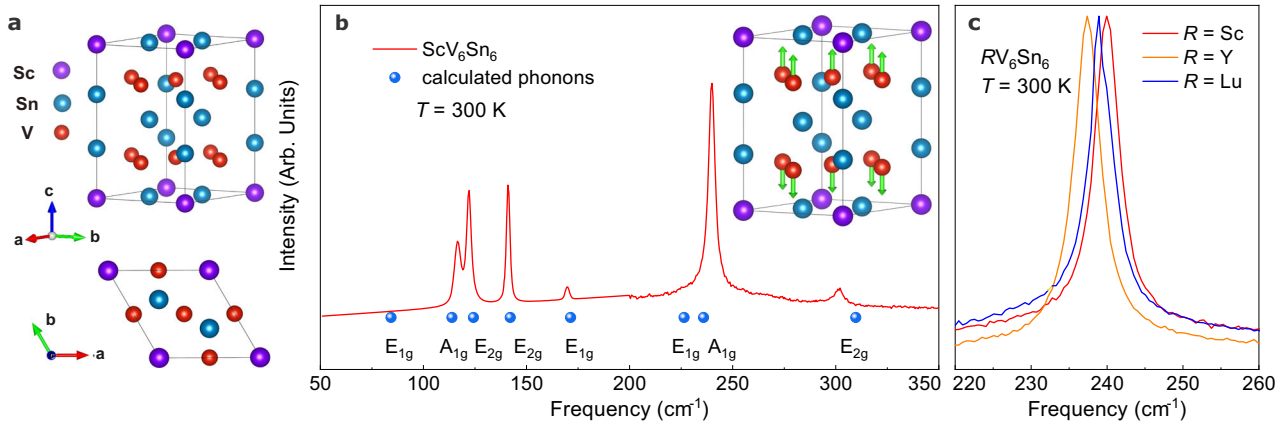

Fig. 1 Properties of hexagonal ScV_6Sn_6 at room temperature. a Crystal structure of ScV_6Sn_6 (space group *P6/mmm*, #191)[25]. This three dimensional material hosts two vanadium kagomé layers separated by $ScSn_2$ and Sn_2 layers along the out-of-plane direction. **b** Raman scattering spectrum of ScV_6Sn_6 compared with predictions from complementary lattice dynamics calculations. The spectrum is collected on the *ab* plane in the back-scattering geometry. The inset shows the displacement pattern of the A_{1g} symmetry mode near 240 cm^{-1}. **c** Close up view of the phonon near 240 cm^{-1} in the RV_6Sn_6 family materials (R = Sc, Y, Lu).

Both of these instabilities are comprised of mostly out-of-plane Sc displacements, and they lead to metastable phases with competing energies[33]. Hence, elucidating phonon behavior across the CDW transition is important to understanding CDW phase stability in this system.

In this work, we combine temperature- and pressure-dependent Raman scattering spectroscopy of ScV_6Sn_6 with complementary lattice dynamics calculations to reveal the properties of the charge density wave states in this model bi-layer kagomé metal. What distinguishes our work from prior efforts[40] is the quality of our single crystals with different R site substitutions, the ability to employ both temperature and pressure as tuning parameters, and our symmetry-guided strategy of projecting the high temperature phase *P6/mmm* phonons onto those in the low temperature CDW state to uncover their origins. We find that the A_{1g} symmetry mode near 240 cm^{-1} - which involves out-of-plane V center motion - is very sensitive to the development of the CDW. For instance, even though it corresponds to a singly-degenerate phonon mode, it seemingly displays five-fold splitting in the low temperature phase consistent with $R\bar{3}m$ symmetry. We discuss this multiplet structure in terms of mixing of nearby symmetry-appropriate and zone-folded phonons, specifically those of A_{1g}, E_g, and P symmetries. We also demonstrate that compression at room temperature may quench the recently reported short-range CDW in ScV_6Sn_6 but has no effect on the Lu analog. We therefore establish that density wave stability is impacted by both physical and chemical pressure. These findings revise our understanding of phonons and their mixing processes in ScV_6Sn_6 related materials.

RESULTS AND DISCUSSION

Raman-active phonons of ScV_6Sn_6 at 300 K

Figure 1b summarizes the Raman scattering response of ScV_6Sn_6 at room temperature. We employ a symmetry analysis, complementary lattice dynamics calculations, polarizer/analyzer combinations, and chemical substitution on the R site to assign the excitations. Overall, the eight calculated phonon frequencies (blue spheres in Fig. 1b, see Supplementary Table 2) are in excellent agreement with the measured spectrum. Challenging assignments are near 240 cm^{-1} where there are two candidate modes and below 200 cm^{-1} where the Raman-active phonons are embedded in a series of extra peaks (Supplementary Fig. 1a). The latter turn out to be rotational modes of air in the optical path. They appear in this and other measurements of ScV_6Sn_6[40,41] due to the low brightness of the sample but can be omitted by purging the optical path and by using standard oscillator-fitting techniques as we did here. The peak near 240 cm^{-1} is important to our continuing discussion. According to our lattice dynamics calculations, there are two candidates for this structure: E_{1g} and A_{1g} symmetry modes. Surprisingly, the peak can be fit by a single oscillator suggesting that one of these constituents is present with extremely low intensity. Based upon extinction behavior under various polarizer/analyzer arrangements [Supplementary Fig. 1b], we assign the 240 cm^{-1} peak as primarily an A_{1g} symmetry mode. The E_{1g} mode is essentially undetectable due to its low intensity. The displacement pattern of the A_{1g} symmetry mode, which involves out-of-plane V center motion, is shown in the inset of Fig. 1b. Substitution on the rare earth site is less useful for assignment purposes because the frequency vs. mass trend is not straightforward [Fig. 1c]. The atomic radius of the R center and the precise local environment appear to be more important. The complete set of mode displacement patterns in ScV_6Sn_6 is given in Supplementary Table 1.

Spectral changes across the CDW transition

Figure 2a summarizes the Raman scattering response of ScV_6Sn_6 as a function of temperature in the high frequency region. We focus on the behavior of the A_{1g} symmetry mode near 240 cm^{-1}. This structure hardens systematically with decreasing temperature and appears to split into a cluster of at least five closely-spaced peaks below 90 K. (The low brightness of this sample and resolution issues make it difficult to tell whether the small shoulders and tiny features on the baseline are real - sufficiently different from nearby peaks as well as the noise level.) This cluster is the most conspicuous signature of the CDW phase, although it obviously raises questions of exactly how and why a singly-degenerate vibrational mode might split in a low symmetry environment. We show the behavior of the E_{2g} phonon near 300 cm^{-1} for comparison. This structure hardens anharmonically with decreasing temperature but does not split across T_{CDW} - in line with the other Raman-active modes in ScV_6Sn_6 including those of A_{1g} symmetry. Complementary measurements of LuV_6Sn_6 and YV_6Sn_6 reveal no low temperature fine structure near 240 cm^{-1} [Supplemental Fig. 2], consistent with transport results indicating the absence of CDW transitions in the R = Lu and Y analogs[21,23]. This demonstrates that the new cluster of peaks near the A_{1g} symmetry mode is a signature of the unusual CDW state in ScV_6Sn_6.

We quantify these results by fitting the Raman scattering response of ScV_6Sn_6 with a series of Voigt oscillators and a linear

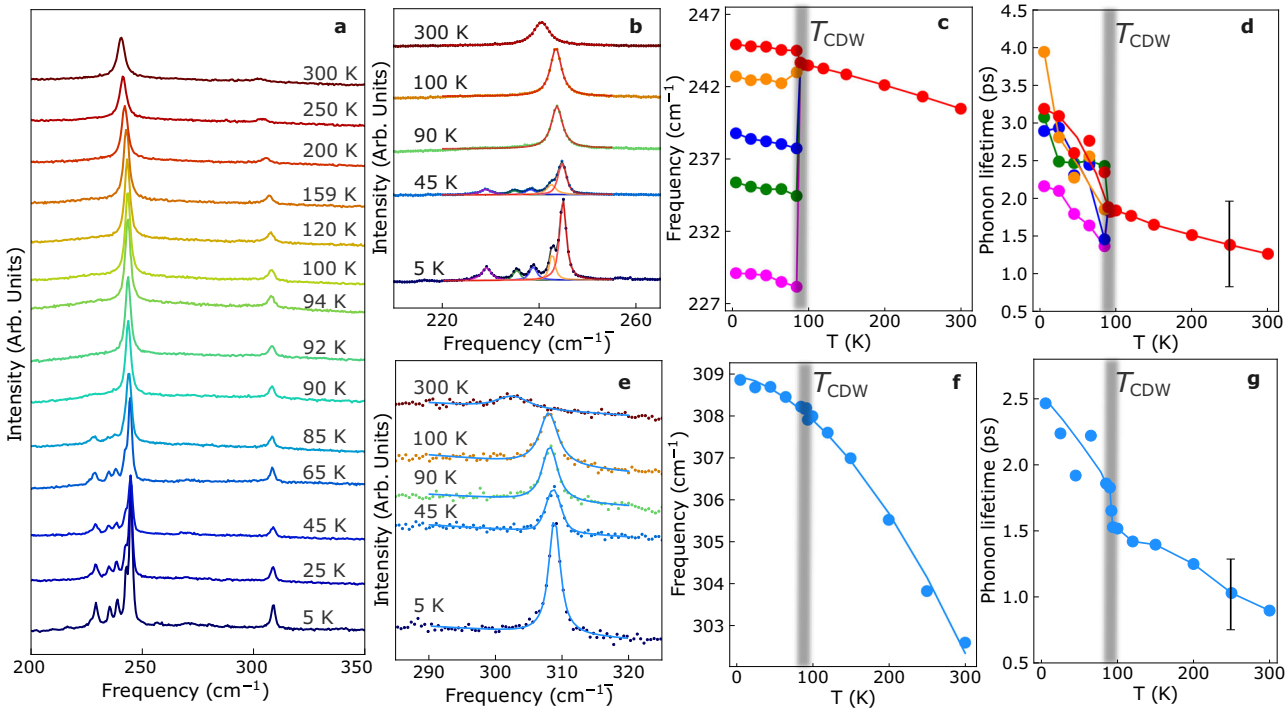

Fig. 2 Symmetry breaking across the CDW transition in ScV_6Sn_6. a Summary of the Raman-active modes near 240 and 300 cm^{-1} as a function of temperature. All the spectra are collected on the *ab* plane in the back-scattering geometry. **b** Close-up view of the spectra at selected temperatures along with an oscillator fit. Several new features emerge in the CDW phase due to symmetry breaking. A minimum of five Voigt oscillators are needed to model the base temperature data. **c**, **d** Frequency vs. temperature and phonon lifetime vs. temperature trends for the features near 240 cm^{-1}. These findings were extracted from the results in (**b**). In (**c**), error bars are on the order of the symbol size; a characteristic error bar is indicated in (**d**). **e** Close-up view of the E_{2g} symmetry mode near 300 cm^{-1} as a function of temperature. This mode can be fit with a single Voigt oscillator over the full temperature range. **e**, **f** Frequency vs. temperature and phonon lifetime vs. temperature trends for the E_{2g} symmetry mode near 300 cm^{-1}. In (**f**) error bars are on the order of the symbol size; a characteristic error bar is shown in (**g**).

baseline. Close-up views of the modes of interest along with their oscillator fits are shown in Fig. 2b, e. A single oscillator is required to fit the A_{1g} symmetry mode in the normal state, whereas a minimum of five oscillators are needed to fit the spectra in the CDW state. By contrast, a single oscillator fits the E_{2g} mode near 300 cm^{-1} over the full temperature range. The center frequency and full width at half maximum (FWHM) are extracted from these fits. The phonon lifetime τ is a useful quantity related to the Heisenberg uncertainty principle that can be calculated as $\tau = \hbar/\mathrm{FWHM}$[42].

Figure 2c, d displays frequency and phonon lifetime trends as a function of temperature for the A_{1g} symmetry phonon. The sharp peaks that develop immediately below T_{CDW} are consistent with a first-order phase transition[25,30–32], although as we shall see below, the multiplet structure is not due to symmetry breaking-induced splitting because a singly-degenerate vibrational mode cannot not split further as part of a group-subgroup transition. At the same time, the strong clustering seems to argue against the appearance of traditional zone-folded phonons unless the phonon bands are rather flat and fold into a similar frequency window[37,43,44]. Overall, the phonon lifetime rises from 1.25 ps at room temperature to between 2.2 and 4 ps in the low temperature phase depending on the branch.

Figure 2f, g displays frequency and phonon lifetime of the E_{2g} phonon as a function of temperature. The mode hardening can be modeled by characteristic anharmonic effects[45] where $\omega(T) = \omega_0 + A(1+\frac{2}{e^x-1}) + B(1+\frac{3}{e^y-1}+\frac{3}{(e^y-1)^2})$ with $x = \hbar\omega_0/2k_BT$, $y = \hbar\omega_0/3k_BT$. Here, ω_0 is the characteristic frequency at base temperature, A and B are constants. There are no anomalies in the frequency vs. temperature curve near the CDW transition. On the other hand, the phonon lifetime shows a pronounced kink at T_{CDW}, rising sharply toward a limiting low temperature value of 2.5 ps. We carried out a similar analysis of the lower frequency phonons in ScV_6Sn_6 as well. No additional fine structure or unusual phonon softening was identified within our sensitivity, although we emphasize that ScV_6Sn_6 is a very low brightness sample. Thus, the new set of peaks near 240 cm^{-1} is the most reliable for unraveling phonon mixing in the CDW state.

Phonon mixing in the low temperature phase of ScV_6Sn_6

In order to better understand the multiplet structure of the 240 cm^{-1} phonon, we performed a symmetry analysis of the phonon modes[46]. In particular, we solved the *subduction* problem which relates the irreducible representations of the high-temperature *P6/mmm* structure and the low-temperature $R\bar{3}m$ structure [Table 1]. This is a powerful technique that unravels a set of perturbed modes in terms of unperturbed vibrational modes[47,48]. As an aside, while we are aware that other studies have identified the CDW structure as belonging to the *R*32 space group[25], our DFT results suggest $R\bar{3}m$ is more likely (see Supplementary Information for additional discussion). As expected, A_{1g} irreducible representations in *P6/mmm*, which exhibit the full crystal symmetry of the *P6/mmm* structure, also exhibit the full crystal symmetry of the subgroup $R\bar{3}m$. They thus map to A_{1g} in $R\bar{3}m$ as well. This irreducible representation is Raman-active in both structures, but is only one-dimensional - a single A_{1g} peak at 240 cm^{-1} in the high-temperature structure *cannot*, on its own, account for all five new modes in the $R\bar{3}m$ structure. Where, then, do the new modes come from?

The results in Table 1 reveal that new Raman active modes can appear in $R\bar{3}m$ from the B_{1g} modes of *P6/mmm* at the zone center, as well as P_1 and P_3 modes which fold in to Γ from the $P \equiv (\frac{1}{3}, \frac{1}{3}, \frac{1}{3})$ point on the Brillouin zone boundary in reciprocal space (defined in Supplementary Table 3). In order to gain a quantitative understanding of the origin of each mode, we calculate the phonons in the $R\bar{3}m$ structure (with frequencies given in Supplementary Table 5), then perform an analysis where the eigenvectors of the dynamical matrix associated with each phonon mode in the $R\bar{3}m$ structure are projected onto the eigenvectors of the dynamical matrix in the *P6/mmm* structure as described in the Methods section. While all symmetry-allowed *P6/mmm* phonon modes are allowed to mix in the formation of the $R\bar{3}m$ phonon modes (for example, a given $R\bar{3}m$ A_{1g} mode could exhibit significant contributions from multiple *P6/mmm* A_{1g}, B_{1g}, and P_1 modes simultaneously), this technique allows us to understand the relative magnitudes of those contributions.

Table 1. Subduction relations between the high-temperature *P6/mmm* and low-temperature $R\bar{3}m$ structures.

P6/mmm		$R\bar{3}m$
$\boldsymbol{A_{1g}/\Gamma_1^+}$	→	$\boldsymbol{A_{1g}/\Gamma_1^+}$
B_{1g}/Γ_4^+	→	$\boldsymbol{A_{1g}/\Gamma_1^+}$
$\boldsymbol{E_{1g}/\Gamma_6^+}$	→	$\boldsymbol{E_g/\Gamma_3^+}$
$\boldsymbol{E_{2g}/\Gamma_5^+}$	→	$\boldsymbol{E_g/\Gamma_3^+}$
P_1	→	$\Lambda_1 + \boldsymbol{A_{1g}/\Gamma_1^+} + A_{2u}/\Gamma_2^-$
P_3	→	$\Lambda_3 + E_u/\Gamma_3^- + \boldsymbol{E_g/\Gamma_3^+}$

We only list the irreps of the high-symmetry structure that lead to Raman-active irreps in the low-temperature $R\bar{3}m$ structure. Raman active irreps are highlighted in bold. For the zone-center modes, we list both the space group irrep (for example Γ_1^+ and the corresponding point group irrep (such as A_{1g}.) Irrep labels P_i refer to irreps at the $P \equiv (\frac{1}{3}, \frac{1}{3}, \frac{1}{3})$ point in reciprocal space for the *P6/mmm* structure; our definition of these irreps are included in Supplementary table 3 and 4 (our notation matches that found on the Bilbao Crystallographic Server).

Figure 3 shows that eight Raman-active $R\bar{3}m$ modes in the 228 to 241 cm^{-1} range exhibit significant overlap with A_{1g}, E_{1g}, P_1, and P_3 phonons in the 220 to 235 cm^{-1} range in the *P6/mmm* structure. Thus, the five clear peaks that abruptly appear alongside of the A_{1g} peak at 240 cm^{-1} are likely a subset of these eight modes, and therefore originate not just from the A_{1g} peak at 240 cm^{-1}, but from E_{1g} modes as well as modes at the *P* point in reciprocal space which fold into the Γ point and become Raman-active in the $R\bar{3}m$ structure. In other words, we attribute the formation of multiplet structure in the CDW state to contributions from the A_{1g} and E_{1g} modes, which also undergo hybridization with *P* modes. It is noteworthy that the A_{1g} mode near 240 cm^{-1} is unique as it is the only observable feature in the high temperature phase that also contributes to the formation of the five peaks in the CDW state. This indicates that the A_{1g} phonon plays a peculiar and as-yet not fully-defined role in the process. One possibility is that the A_{1g} mode couples strongly with the CDW modes, as it does in CsV_3Sb_5[39], and hence plays an important role in the stabilization of the *P* point CDW mode[25].

Pressure destabilizes the CDW state

Figure 4 summarizes the Raman scattering response of ScV_6Sn_6 under pressure at room temperature. We focus on the behavior of the A_{1g} symmetry phonon near 240 cm^{-1} because (i) it is most strongly connected to the CDW state and (ii) all other modes show only simple hardening under compression - at least within our sensitivity. As indicated in Fig. 4a, b, this peak can be modeled with a single oscillator below 2 GPa and also above approximately 6 GPa. At intermediate pressures, the spectra of ScV_6Sn_6 are best fit with two Voigt oscillators indicating the presence of a mixed phase. This type of mixed or two-phase regime is typical for a first-order pressure-driven transition[49]. In our case, the mixed phase consists of *P6/mmm* + a new high

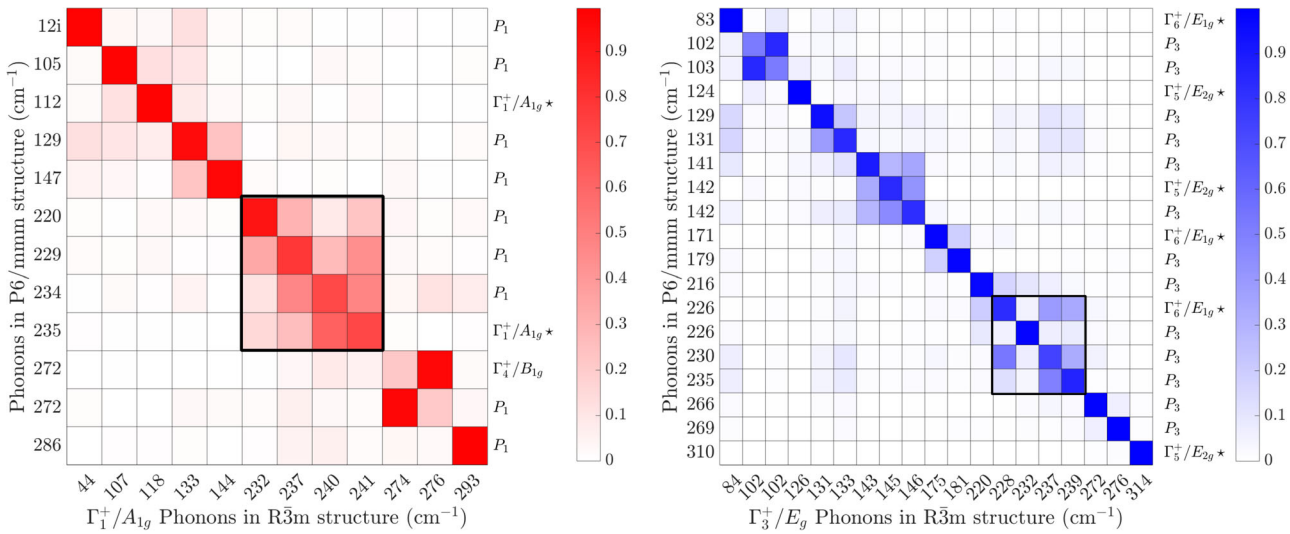

Fig. 3 Overlap of eigenvectors of the dynamical matrix between phonons in the P6/mmm structure (vertical axis) and phonons in the R$\bar{3}$m structure (horizontal axis). The color intensity of each box denotes the magnitude of the overlap, with a maximum possible amplitude of unity. The lefthand panel corresponds to projections of *P6/mmm* phonons transforming as A_{1g}, B_{1g}, and P_1 onto $R\bar{3}m$ phonons transforming as A_{1g}, while the right-hand panel corresponds to projections of *P6/mmm* phonons transforming as E_{1g}, E_{2g}, and P_1 onto $R\bar{3}m$ phonons transforming as E_g. Taken together, these two panels include all Raman-active phonon modes in the $R\bar{3}m$ structure, as well as all *P6/mmm* phonon modes related to them through subduction [Table 1]. Raman active modes in the *P6/mmm* structure are denoted with a "⋆" character. In both panels, the area of interest corresponding to phonons from 228 cm^{-1} to 241 cm^{-1} in the $R\bar{3}m$ structure are boxed. Note that the data as presented need not be symmetric.

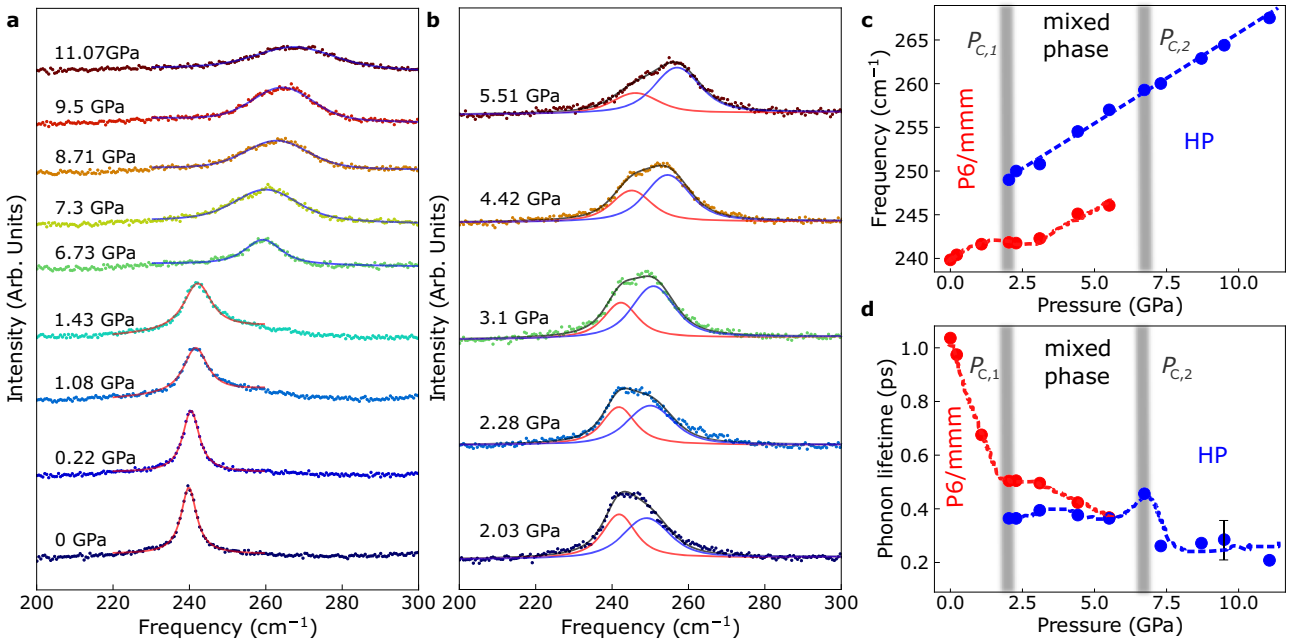

Fig. 4 Pressure-driven structural phase transition in ScV_6Sn_6 at room temperature. a, **b** Raman scattering response as a function of pressure. The dotted lines are experimental data, and the solid lines correspond to fitted curves. **c**, **d** Raman shift and phonon lifetime as a function of pressure for the 240 cm^{-1} phonon. Two critical pressures ($P_{C,1} = 2$ GPa and $P_{C,2} = 6$ GPa) separate the *P6/mmm* phase, the mixed phase, and the high pressure (HP) phase. The error bars in (**c**) are on the order of the symbol size; a characteristic error bar is indicated in (**d**).

pressure phase. Based on this behavior, we define two critical pressures: $P_{C,1} = 2$ GPa and $P_{C,2} = 6$ GPa.

Figure 4c, d displays frequency vs. pressure and phonon lifetime trends for ScV_6Sn_6. We find that the concentration of *P6/mmm* (as measured by the relative strength of the low frequency oscillator) diminishes with increasing compression in the mixed phase region whereas that of the new high pressure phase (measured by the relative strength of the second peak) increases until it dominates above $P_{C,2}$. The high pressure phase of ScV_6Sn_6 is very similar to but not identical to *P6/mmm*. The single A_{1g}-like phonon mode emerging above $P_{C,2}$ has a higher frequency than that in the *P6/mmm* ground state, pointing to a stronger force constant as well as a volume reduction in the high pressure phase which may have interesting connections to the inter-layer coupling in this class of kagomé metals. At the same time, the phonon lifetime drops from 1 ps at ambient pressure (lower than most traditional semiconductors and chalcogenides) to approximately 0.2 ps over this range. The decreased lifetime is due to significantly increased scattering events under compression[42]. We mention in passing that we could not stabilize the high pressure phase in our first principles simulations under pressure. This may be due to complications from the residual density wave state recently reported at room temperature[31,32] or a shortcoming of density functional theory.

We postulate the following link between the pressure-driven transition in Fig. 4 and density wave stability in this material. One key fact is that recent transport work in the low temperature phase of ScV_6Sn_6 reveals complete suppression of the long-range CDW at approximately 2.4 GPa[24]. It is tempting to claim that this destabilization corresponds to the region between $P_{C,1}$ and $P_{C,2}$, but we must remember that our measurements are performed at room temperature - where the CDW is not fully developed. The recently reported short-range CDW builds upon this finding and provides a way forward. This "residual CDW" resides in the high temperature phase of ScV_6Sn_6 and hosts a (1/3, 1/3, 1/2) propagation vector[31,32]. As there are no high pressure structural phases stabilized in our first-principles simulations and no other orders present at room temperature in ScV_6Sn_6, we hypothesize that pressure quenches short-range CDW correlations in the high temperature phase of this system as well. It appears to do so in a first-order mixed phase manner[49] between $P_{C,1}$ and $P_{C,2}$.

We tested this hypothesis using crystals with different rare earth centers. The crucial result is that similar high pressure Raman scattering measurements on the Lu analog reveal no evidence for the type of behavior observed in ScV_6Sn_6. Instead, the A_{1g} symmetry mode near 240 cm^{-1} hardens systematically under compression [Supplementary Fig. 3] in line with the fact that LuV_6Sn_6 does not host a CDW[50] and therefore does not host pressure-induced destabilization of a short range CDW at room temperature. These structure-property relations are nicely unified by *R* site size arguments [Inset, Supplementary Fig. 1c] which reveal that both chemical and physical pressure drive similar trends in CDW stability. In this scenario, the behavior of the A_{1g} mode potentially signals the development of both long- and short-range CDW order.

There are few parallels between the pressure-induced transition in ScV_6Sn_6 and those observed in the single-layer vanadate kagomés like AV_3Sb_5. This is because the latter takes place at low temperature and between two different long-range-ordered CDW phases and the high symmetry phase, whereas in ScV_6Sn_6 this transition takes place at room temperature, well above the long-range CDW order[39,51,52]. An alternate possibility that accounts for the disappearance of the CDW at high pressures is that the system undergoes a volume collapse transition similar to those observed in the $ThCr_2Si_2$ family of compounds, which involves the formation of Sn–Sn covalent bonds[53,54]. Such transitions are also observed in various iron-pnictide superconductors, and couple strongly to superconductivity because of their effect on the Fermi surface[55,56]. While it may be too early for a full physical picture to emerge due to the limited number of measurements of ScV_6Sn_6 under compression, such a transition - if it exists - is likely to suppress the CDW as well. We note,

however, that there is no evidence for Sn–Sn bond formation in our spectra, making this scenario less likely.

Unraveling CDW stability in the RV_6Sn_6 family of materials (R = Sc, Y, Lu)

In this family of materials, most of the focus so far has been on the electronic properties[38,40,57–59]. There has been significantly less effort to uncover vibrational contributions to the mechanism. This is partly because metallic character in both high and low temperature phases of ScV_6Sn_6 prevents us from revealing the behavior of the infrared-active phonons due to screening by the Drude peak[34]. The Raman scattering response is, however, still accessible[35], and combined with different external stimuli and complementary lattice dynamics calculations, a remarkable picture of phonon mixing is beginning to emerge.

In this work, we traced how phonons mix in the CDW state of the double-layer vanadate ScV_6Sn_6, tested these ideas with symmetry arguments based upon our lattice dynamics calculations, and compared our findings to behavior in the Y and Lu analogs. Overall, we demonstrate that low temperature stabilizes the CDW whereas both physical and chemical pressures destroy it. This suggests that the electron-phonon interactions are on the "knife's edge", easily manipulated by any external stimuli and more sensitive than the similar CDW orders in the monolayer AV_3Sb_5 vanadates. Our analysis reveals that the multiplet character near 240 cm^{-1} in the CDW state of ScV_6Sn_6 is due to mixing of $P6/mmm$ and $R\bar{3}m$ phase phonons - a result that we quantify by projecting phonons of the high symmetry state onto those of the lower symmetry structure. We emphasize that these five peaks are not due to symmetry breaking of a single mode in the conventional sense. Instead, this multiplet is a combination of both Γ and P point modes that are folded to the zone center and mixed such that they become Raman active. This process indicates that the density wave state is influenced by a variety of phonon modes and highlights the intricate, phonon-assisted nature of the low temperature phase. Similar phonon hybridization has been observed in CsV_3Sb_5[37]. Since the A_{1g} symmetry phonon near 240 cm^{-1} may also serve to connect the long- and short-range CDWs, it provides a sensitive, microscopic indicator of CDW stability under different tuning parameters.

METHODS

Crystal growth and diamond anvil cell loading

High quality RV_6Sn_6 (R = Sc, Lu, Y) crystals were grown from a Sn-rich melt method with a composition ratio of R:V:Sn = 1:6:60 as described in ref. [25]. They are hexagonal blocks with clear ab surfaces. For the high pressure Raman scattering measurements, a small single crystal was loaded into a symmetric diamond anvil cell suitable for work in the 0–13 GPa range. The cell is equipped with low fluorescence diamonds with 400 μm culets. We also employed a stainless steel gasket with a 100 μm hole, KBr as the pressure medium, and an annealed ruby ball for pressure determination via fluorescence[60].

Raman spectroscopy

Raman scattering measurements were performed in the back scattering geometry using a Horiba LabRAM HR Evolution spectrometer equipped with a 532 nm (green) laser, a 50× microscope objective, 1800 line/mm gratings, and a liquid-nitrogen-cooled charge-coupled device detector. To minimize heating and maximize signal intensity for this low brightness sample, power was controlled below 7.7 mW, and the laser was slightly defocused. Each spectrum was integrated for 200 s and averaged four times. Variable temperature work was carried out with a low-profile open-flow cryostat, and high pressure measurements employed a diamond anvil cell as described above. Standard peak fitting techniques were employed as appropriate.

Lattice dynamics calculations

All density functional theory (DFT) calculations were performed with Projector Augmented Waves (PAW) as implemented in the Vienna Ab initio simulation package (VASP) version 5.4.4[61–63] using the PBEsol exchange-correlation functional for valence configurations of Sc, V, and Sn corresponding to $3s^23p^64s^13d^2$, $3s^23p^64s^13d^4$, and $5s^24d^{10}5p^2$, respectively. Unless otherwise mentioned, experimentally determined lattice parameters of $a = 5.475$ Å and $c = 9.177$ Å for the $P6/mmm$ structure and $a = 9.456$ Å and $c = 27.412$ Å for the conventional $R\bar{3}m$ structure were used for all calculations Internal degrees of freedom were relaxed, with forces converged to within 0.001 eV/Å using a plane wave cutoff energy of 400 eV, combined with a Γ-centered Monkhorst-Pack k-point mesh of $20 \times 20 \times 10$ in the $P6/mmm$ structure, as well as a Gaussian smearing parameter of 10 meV. Calculations in the $R\bar{3}m$ structure were carried out in a primitive, three formula-unit cell commensurate with the wavevector $\mathbf{P} = (\frac{1}{3}, \frac{1}{3}, -\frac{1}{3})$, which corresponds to a unit cell with basis vectors $(\frac{2}{3}, \frac{1}{3}, \frac{1}{3}), (-\frac{1}{3}, \frac{1}{3}, \frac{1}{3}), (-\frac{1}{3}, -\frac{2}{3}, \frac{1}{3})$, where the indices (a, b, c) correspond to the lattice vectors of the conventional $R\bar{3}m$ nine formula unit cell. All computational parameters used for this structure were the same as for the $P6/mmm$ structure, except with a Γ-centered Monkhorst-Pack k-point mesh of $10 \times 10 \times 10$. To calculate phonon frequencies and their associated distortions, we constructed the dynamical matrix in a basis of symmetry adapted modes, which bring the dynamical matrix into block diagonal form, where each block corresponds to a single irreducible representation of the space group. These symmetry-adapted linear combinations of atomic displacements were found using the ISOTROPY software suite[64].

Phonon overlap

After calculating the eigenvectors of the dynamical matrix associated with each phonon mode, we then computed the relationship between eigenvectors $\hat{e}_i^{I\alpha}$ in the $P6/mmm$ structure (where I is an irrep, α the mode index within that irrep, and i the ionic degree of freedom in cartesian coordinates), and the eigenvectors $\hat{g}_i^{I\alpha}$ in the $R\bar{3}m$ structure. First, the $\hat{e}_i^{I\alpha}$ were expressed in a three formula unit basis commensurate with the $R\bar{3}m$ cell, then renormalized. The overlap for two phonons is then defined as the projection of $\hat{g}_i^{I\alpha}$ onto $\hat{e}_i^{I\alpha}$,

$$O(J,\beta,I,\alpha) = \sqrt{\left(\hat{g}_i^{J\beta}\hat{e}_i^{I\alpha}\right)^2}. \quad (1)$$

In the left hand panel of Fig. 3, $J = A_{1g}$, and $I \in A_{1g}, B_{1g}, P_1$, as determined by the solution to the subduction problem described in Table 1. In the righthand panel, $J = E_g$, and $I \in E_{1g}, E_{2g}, P_3$. In this second case, the E_{1g} and E_{2g} phonons are doubly degenerate, and the P_3 phonons quadruply degenerate. In order to compress the results of the table, instead of reporting a cell for each individual degenerate mode, our figure includes a single cell with amplitude defined as $\tilde{O}$, where

$$\tilde{O}(J,\beta,I,\alpha) \equiv \frac{1}{M_\beta}\sum_{\beta_I}\sqrt{\sum_{\alpha_m} O(J,\beta_I,I,\alpha_m)^2}. \quad (2)$$

Here, I and m run over the degenerate indices of β and α respectively, and M_β is the multiplicity of the β irrep being projected. Similar approaches have been employed in other materials[47,48].

Group theory

The symmetry-adapted linear combinations of atomic displacements used for the phonon calculations were found using the ISOTROPY software suite[64]. The subduction analysis to find the

connections between irreps through the group-subgroup transition was performed using the CORREL application hosted by the Bilbao crystallographic server[46].

DATA AVAILABILITY

Data used in this study is available from the University of Minnesota Digital Conservatory at https://doi.org/10.13020/bchr-e775.

CODE AVAILABILITY

All custom codes used in this study are available from the University of Minnesota Digital Conservatory at https://doi.org/10.13020/bchr-e775.

Received: 30 April 2023; Accepted: 29 September 2023;
Published online: 13 October 2023

REFERENCES

1. Kang, M. et al. Dirac fermions and flat bands in the ideal kagome metal FeSn. *Nat. Mater.* **19**, 163–169 (2020).
2. Li, M. et al. Dirac cone, flat band and saddle point in kagome magnet YMn_6Sn_6. *Nat. Commun.* **12**, 3129 (2021).
3. Liu, Z. et al. Orbital-selective Dirac fermions and extremely flat bands in frustrated kagome-lattice metal CoSn. *Nat. Commun.* **11**, 4002 (2020).
4. Yin, J.-X. et al. Negative flat band magnetism in a spin–orbit-coupled correlated kagome magnet. *Nat. Phys.* **15**, 443–448 (2019).
5. Meier, W. R. et al. Flat bands in the CoSn-type compounds. *Phys. Rev. B* **102**, 075148 (2020).
6. Balents, L. Spin liquids in frustrated magnets. *Nature* **464**, 199–208 (2010).
7. Yan, S., Huse, D. A. & White, S. R. Spin-liquid ground state of the S= 1/2 kagome Heisenberg antiferromagnet. *Science* **332**, 1173–1176 (2011).
8. Paul, A., Chung, C.-M., Birol, T. & Changlani, H. J. Spin-lattice Coupling and the Emergence of the Trimerized Phase in the S= 1 Kagome Antiferromagnet $Na_2Ti_3Cl_8$. *Phys. Rev. Lett.* **124**, 167203 (2020).
9. Ye, L. et al. Massive Dirac fermions in a ferromagnetic kagome metal. *Nature* **555**, 638–642 (2018).
10. Lachman, E. et al. Exchange biased anomalous Hall effect driven by frustration in a magnetic kagome lattice. *Nat. Commun.* **11**, 560 (2020).
11. Tanaka, M. et al. Topological Kagome magnet $Co_3Sn_2S_2$ thin flakes with high electron mobility and large anomalous Hall effect. *Nano Lett.* **20**, 7476–7481 (2020).
12. Xu, G., Lian, B. & Zhang, S.-C. Intrinsic quantum anomalous hall effect in the kagome lattice $Cs_2LiMn_3F_{12}$. *Phys. Rev. Lett.* **115**, 186802 (2015).
13. Rüegg, A. & Fiete, G. A. Fractionally charged topological point defects on the kagome lattice. *Phys. Rev. B* **83**, 165118 (2011).
14. Feng, Z. et al. Gapped spin-1/2 spinon excitations in a new kagome quantum spin liquid compound $Cu_3Zn(OH)_6FBr$. *Chin. Phys. Lett.* **34**, 077502 (2017).
15. Ghimire, N. J. et al. Competing magnetic phases and fluctuation-driven scalar spin chirality in the kagome metal YMn_6Sn_6. *Sci. Adv.* **6**, eabe2680 (2020).
16. Wang, Q. et al. Field-induced topological Hall effect and double-fan spin structure with a *c*-axis component in the metallic kagome antiferromagnetic compound YMn_6Sn_6. *Phys. Rev. B* **103**, 014416 (2021).
17. Teng, X. et al. Magnetism and charge density wave order in kagome FeGe. *Nat. Phys.* **19**, 814–822 (2023).
18. Ortiz, B. R. et al. New kagome prototype materials: discovery of KV_3Sb_5, RbV_3Sb_5, and CsV_3Sb_5. *Phys. Rev. Mater.* **3**, 094407 (2019).
19. Ortiz, B. R. et al. CsV_3Sb_5: A $\mathbb{Z}_2$ topological kagome metal with a superconducting ground state. *Phys. Rev. Lett.* **125**, 247002 (2020).
20. Teng, X. et al. Discovery of charge density wave in a kagome lattice antiferromagnet. *Nature* **609**, 490–495 (2022).
21. Pokharel, G. et al. Electronic properties of the topological kagome metals YV_6Sn_6 and YV_6Sn_6. *Phys. Rev. B* **104**, 235139 (2021).
22. Hu, Y. et al. Tunable topological Dirac surface states and van Hove singularities in kagome metal GdV_6Sn_6. *Sci. Adv.* **8**, eadd2024 (2022).
23. Zhang, X. et al. Electronic and magnetic properties of intermetallic kagome magnets $RV_6Sn_6 (R = \mathrm{Tb} - \mathrm{Tm})$. *Phys. Rev. Mater.* **6**, 105001 (2022).
24. Zhang, X. et al. Destabilization of the charge density wave and the absence of superconductivity in ScV_6Sn_6 under high pressures up to 11 GPa. *Materials* **15**, 7372 (2022).
25. Arachchige, H. W. S. et al. Charge density wave in kagome lattice intermetallic ScV_6Sn_6. *Phys. Rev. Lett.* **129**, 216402 (2022).
26. Ritz, E. T. et al. Superconductivity from Orbital-Selective Electron-Phonon Coupling in AV_3Sb_5. *Phys. Rev. B* **108**, L100510 (2023).
27. Zhao, H. et al. Cascade of correlated electron states in the kagome superconductor CsV_3Sb_5. *Nature* **599**, 216–221 (2021).
28. Liang, Z. et al. Three-dimensional charge density wave and surface-dependent vortex-core states in a kagome superconductor CsV_3Sb_5. *Phys. Rev. X* **11**, 031026 (2021).
29. Du, F. et al. Pressure-induced double superconducting domes and charge instability in the kagome metal KV_3Sb_5. *Phys. Rev. B* **103**, L220504 (2021).
30. Hu, T. et al. Optical spectroscopy and band structure calculations of the structural phase transition in the vanadium-based kagome metal ScV_6Sn_6. *Phys. Rev. B* **107**, 165119 (2023).
31. Cao, S. et al. Competing charge-density wave instabilities in the kagome metal ScV_6Sn_6. *Preprint at* https://doi.org/10.48550/arXiv.2304.081977 (2023).
32. Korshunov, A. et al. Softening of a flat phonon mode in the kagome ScV_6Sn_6. *Preprint at* https://doi.org/10.48550/arXiv.2304.091733 (2023).
33. Tan, H. & Yan, B. Abundant Lattice Instability in Kagome Metal ScV_6Sn_6. *Phys. Rev. Lett.* **130**, 266402 (2023).
34. Fan, S. et al. Electronic chirality in the metallic ferromagnet $Fe_{1/3}TaS_2$. *Phys. Rev. B* **96**, 205119 (2017).
35. Fan, S. et al. Excitations of intercalated metal monolayers in transition metal dichalcogenides. *Nano Lett.* **21**, 99–106 (2020).
36. Wu, S. et al. Charge density wave order in the kagome metal $AV_3Sb_5 (A = \mathrm{Cs}, \mathrm{Rb}, \mathrm{K})$. *Phys. Rev. B* **105**, 155106 (2022).
37. Liu, G. et al. Observation of anomalous amplitude modes in the kagome metal CsV_3Sb_5. *Nat. Commun.* **13**, 3461 (2022).
38. Lee, S. et al. Nature of charge density wave in kagome metal ScV_6Sn_6. *Preprint at* https://doi.org/10.48550/arXiv.2304.11820 (2023).
39. Ritz, E. T., Fernandes, R. M. & Birol, T. Impact of Sb degrees of freedom on the charge density wave phase diagram of the kagome metal CsV_3Sb_5. *Phys. Rev. B* **107**, 205131 (2023).
40. Hu, Y. et al. Phonon promoted charge density wave in topological kagome metal ScV_6Sn_6. *Preprint at* https://doi.org/10.48550/arXiv.2304.06431 (2023).
41. Ohno, H., Iizuka, Y. & Fujita, S. Pure rotational raman spectroscopy applied to N_2/O_2 analysis of air bubbles in polar firn. *J. Glaciol.* **67**, 903–908 (2021).
42. Sun, Q.-C. et al. Spectroscopic determination of phonon lifetimes in rhenium-doped MoS_2 nanoparticles. *Nano Lett.* **13**, 2803–2808 (2013).
43. Joshi, J. et al. Short-range charge density wave order in $2H - TaS_2$. *Phys. Rev. B* **99**, 245144 (2019).
44. Hill, H. M. et al. Phonon origin and lattice evolution in charge density wave states. *Phys. Rev. B* **99**, 174110 (2019).
45. Balkanski, M., Wallis, R. F. & Haro, E. Anharmonic effects in light scattering due to optical phonons in silicon. *Phys. Rev. B* **28**, 1928–1934 (1983).
46. Aroyo, M. I., Kirov, A., Capillas, C., Perez-Mato, J. & Wondratschek, H. Bilbao Crystallographic Server. II. Representations of crystallographic point groups and space groups. *Acta Cryst.* **62**, 115–128 (2006).
47. Long, V. C. et al. Far-infrared vibrational properties of high-pressure high-temperature C_{60} polymers and the C_{60} dimer. *Phys. Rev. B* **61**, 13191–13201 (2000).
48. Zhu, Z.-T. et al. Far-infrared vibrational properties of tetragonal C_{60} polymer. *Phys. Rev. B* **65**, 085413 (2002).
49. Musfeldt, J., Mandrus, D. & Liu, Z. Insulator–metal transition in $CrSiTe_3$ triggered by structural distortion under pressure. *npj 2D Mater. Appl.* **7**, 28 (2023).
50. Lee, J. & Mun, E. Anisotropic magnetic property of single crystals RV_6Sn_6 (R = Y, Gd-Tm, Lu). *Phys. Rev. Mater.* **6**, 083401 (2022).
51. Zhang, Z. et al. Pressure-induced reemergence of superconductivity in the topological kagome metal CsV_3Sb_5. *Phys. Rev. B* **103**, 224513 (2021).
52. Gupta, R. et al. Two types of charge order with distinct interplay with superconductivity in the kagome material CsV_3Sb_5. *Commun. Phys.* **5**, 232 (2022).
53. Hoffmann, R. & Zheng, C. Making and breaking bonds in the solid state: The $ThCr_2Si_2$ structure. *J. Phys. Chem.* **89**, 4175–4181 (2002).
54. Foroozani, N. et al. Hydrostatic high-pressure studies to 25 GPa on the model superconducting pnictide $LaRu_2P_2$. *J. Phys.: Conf. Ser.* **500**, 032007 (2014).
55. Kreyssig, A. et al. Pressure-induced volume-collapsed tetragonal phase of $CaFe_2As_2$ as seen via neutron scattering. *Phys. Rev. B* **78**, 184517 (2008).
56. Saha, S. et al. Structural collapse and superconductivity in rare-earth-doped $CaFe_2As_2$. *Phys. Rev. B* **85**, 024525 (2012).
57. Cheng, S. et al. Nanoscale visualization and spectral fingerprints of the charge order in ScV_6Sn_6 distinct from other kagome metals. *Preprint at* https://doi.org/10.48550/arXiv.2302.122277 (2023).
58. Kang, S.-H. et al. Emergence of a new band and the Lifshitz transition in kagome metal ScV_6 Sn_6 with charge density wave. *Preprint at* https://doi.org/10.48550/arXiv.2302.14041 (2023).
59. Tuniz, M. et al. Dynamics and resilience of the charge density wave in a bilayer kagome metal. *Preprint at* https://doi.org/10.48550/arXiv.2302.10699 (2023).

60. Mao, H., Bell, P., Shaner, J. T. & Steinberg, D. Specific volume measurements of Cu, Mo, Pd, and Ag and calibration of the ruby R1 fluorescence pressure gauge from 0.06 to 1 Mbar. *J. Appl. Phys.* **49**, 3276–3283 (1978).
61. Kresse, G. & Hafner, J. Ab initio molecular dynamics for liquid metals. *Phys. Rev. B* **47**, 558 (1993).
62. Kresse, G. & Furthmüller, J. Efficiency of ab-initio total energy calculations for metals and semiconductors using a plane-wave basis set. *Comput. Mater. Sci.* **6**, 15–50 (1996).
63. Kresse, G. & Furthmüller, J. Efficient iterative schemes for ab initio total-energy calculations using a plane-wave basis set. *Phys. Rev. B* **54**, 11169 (1996).
64. Stokes, H., Hatch, D. & Campbell, B. ISOTROPY Software Suite v. 9.6.1. *iso.byu.edu* (2022).

ACKNOWLEDGEMENTS

Work at Tennessee (Y.G., K.A.S., A.L.B., and J.L.M.) is supported by Physical Behavior of Materials, Basic Energy Sciences, U.S. Department of Energy (Contract number DE-SC00023144). W.R.M. and D.M. acknowledge support from the Gordon and Betty Moore Foundation's EPiQS Initiative, Grant GBMF9069 to D.M. R.P.M. and S.M. acknowledge support from the AFOSR MURI (Novel Light-Matter Interactions in Topologically Non-Trivial Weyl Semimetal Structures and Systems), Grant No. FA9550-20-1-0322. Work at the University of Minnesota (E.T.R. and T.B.) was supported by NSF CAREER grant DMR-2046020.

AUTHOR CONTRIBUTIONS

Y.G. and J.L.M. designed the study. W.R.M., S.M., and R.P.M. grew the crystals with guidance from D.G.M.; A.L.B. carried out feasibility measurements while Y.G. performed the variable temperature and high pressure Raman scattering spectroscopy. E.R. performed the theoretical calculations and discussed the results with T.B.; Y.G. and K.A.S. analysed the spectral data with guidance from J.L.M.; Y.G., E.R., and J.L.M. wrote the manuscript. All authors commented on the text.

COMPETING INTERESTS

The authors declare no competing interests.

ADDITIONAL INFORMATION

Supplementary information The online version contains supplementary material available at https://doi.org/10.1038/s41535-023-00590-7.

Correspondence and requests for materials should be addressed to Janice L. Musfeldt.

Reprints and permission information is available at http://www.nature.com/reprints

Publisher's note Springer Nature remains neutral with regard to jurisdictional claims in published maps and institutional affiliations.